

Oceanic transform fault seismicity and slip mode influenced by seawater infiltration

Arjun Kohli¹✉, Monica Wolfson-Schwehr², Cécile Prigent³ and Jessica M. Warren⁴✉

Oceanic transform faults that offset mid-ocean ridges slip through earthquakes and aseismic creep. The mode of slip varies with depth and along strike, with some fault patches that rupture in large, quasi-periodic earthquakes at temperatures <600 °C, and others that slip through creep and microearthquakes at temperatures up to 1,000 °C. Rocks from both fast- and slow-slipping transforms show evidence of interactions with seawater up to temperatures of at least 900 °C. Here we present a model for the mechanical structure of oceanic transform faults based on fault thermal structure and the impacts of hydration and metamorphic reactions on mantle rheology. Deep fluid circulation is accounted for in a modified friction-effective pressure law and in ductile flow laws for olivine and serpentine. Combined with observations of grain size reduction and hydrous mineralogy from high-strain mylonites, our model shows that brittle and ductile deformation can occur over a broad temperature range, 300–1,000 °C. The ability of seawater to penetrate faults determines whether slip is accommodated at depth by seismic asperities or by aseismic creep in weak, hydrous shear zones. Our results suggest that seawater infiltration into ocean transform faults controls the extent of seismicity and spatiotemporal variations in the mode of slip.

Global studies of seismicity^{1–3} and deformation experiments on olivine⁴ suggest that 600–700 °C is the thermal limit for earthquake nucleation on oceanic transform faults (OTFs). However, recent ocean-bottom seismometer (OBS) deployments on fast- and intermediate-slipping transforms have located microearthquakes in the mantle at temperatures up to 1,000 °C in modelled thermal structures^{5–8}. The mode of slip is also observed to vary along-strike, with some fault patches hosting large, quasi-periodic earthquakes while others arrest the propagation of large ruptures and slip through intense swarms of deep microseismicity⁵. Rupture barrier zones show low seismic velocities and high ratios of compressional- to shear-wave velocities indicative of high porosity, which suggests a causal link between hydrological properties and the seismogenic behaviour of the lithosphere^{9,10}. Earthquake cycle models demonstrate that increased dilatancy in these regions can account for observations of slow slip and arrest of large ruptures, but do not explain variations in the vertical extent of microseismicity or along-strike variations in the mode of slip at temperatures >600 °C (ref. ¹¹).

Deformed mantle rocks have been dredged from OTFs that span a wide range of slip rates (Fig. 1a) and provide constraints on the conditions and mechanisms of fault slip. In particular, high-strain mylonites contain syn-deformational hydrous phases, which signify that fluids were present during ductile deformation^{12,13}. Analysis of mylonites from ultra-slow slipping faults on the Southwest Indian Ridge (SWIR) indicates that fluids are derived from seawater and that fluid–rock interactions occur up to at least 900 °C. In this study, we used temperature constraints from the mylonites in combination with numerical models of fault thermal structures to construct rheological profiles of OTFs that incorporate deep seawater circulation and fluid–deformation feedbacks. We then used these models to interpret the OBS observations^{5–8} of along-strike variations in the extent of seismicity and the mode of slip in terms of fault mechanical properties.

OTF mylonites

Mantle mylonites have been dredged from numerous OTFs (Fig. 1a). The presence of syn-deformational hydrous phases in fine-grained shear zones within mylonites indicates that they formed under hydrous conditions (Fig. 1c). We used the hydrous mineralogy to classify mylonites in terms of the temperature of deformation¹³. Low-temperature (LT) mylonites contain amphibole, chlorite and serpentine. Medium-temperature (MT) mylonites contain both amphibole and chlorite. High-temperature (HT) mylonites contain amphibole as the only hydrous phase. LT and HT mylonites with similar characteristics (syn-deformational hydrous phases and very fine grain size compared to that of abyssal peridotites) have been recovered from the fastest- (Garrett) and slowest-slipping (Shaka) transform faults (Supplementary Table 1). The high chlorine content of hydrous minerals in SWIR mylonites (up to 1 wt%) indicates that the fluid source was seawater (Fig. 1e).

The temperature during deformation of LT, MT and HT mylonites can be inferred from the stability fields of hydrous minerals. However, the depth of deformation cannot be directly estimated from mineralogy, as none of the mineral compositions are pressure sensitive. We therefore used fault thermal models to convert temperature constraints into pressure (depth) on the fault (Fig. 2a,b and Extended Table 1). Three-dimensional thermal models were solved for the flow field and thermal structure of the Shaka and Gofar transform faults (Methods). We estimated the temperature on the basis of orthopyroxene composition (Fig. 2c) and compared geotherms from the centre of each fault with the experimentally derived upper stability limits of hydrous minerals^{14–17} to place bounds on the pressure (depth). We designated the LT, MT and HT mylonite regions based on the hydrous mineralogy and used these regions as the bounds on the pressure–temperature conditions of deformation.

¹Department of Geophysics, Stanford University, Stanford, CA, USA. ²Center for Coastal and Ocean Mapping, University of New Hampshire, Durham, NH, USA. ³Institut de Physique du Globe de Paris, Université de Paris, CNRS, Paris, France. ⁴Department of Earth Sciences, University of Delaware, Newark, DE, USA. ✉e-mail: ahkohli@stanford.edu; warrenj@udel.edu

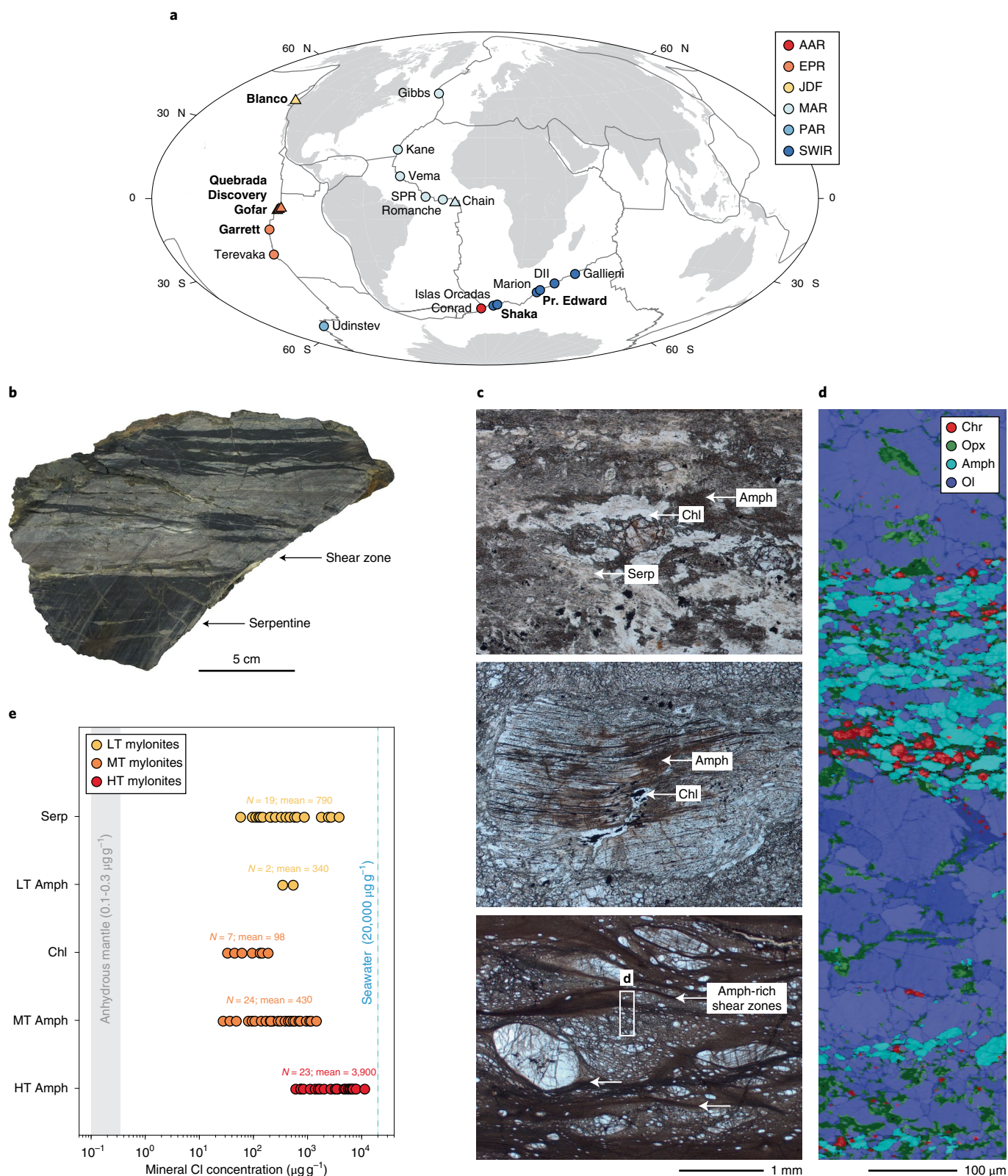


Fig. 1 | Map and microstructures of OTF mylonites. **a**, Global map of OTFs where mylonites have been recovered (circles) and OBS have been deployed (triangles). Bolded faults are discussed in the main text. AAR, American-Antarctic Ridge; MAR, Mid-Atlantic Ridge; PAR, Pacific-Antarctic Ridge. **b**, Serpentinized peridotite mylonite from the fast-slipping Garrett transform fault, EPR. **c**, Photomicrographs (plane polarized light) of HT/MT/LT mylonites from the slow-slipping Shaka transform fault¹². **d**, Electron backscatter diffraction phase map of fine-grained, amphibole-rich bands within a HT mylonite¹². **e**, Chlorine concentrations in hydrous minerals in Shaka and Prince Edward mylonites. Amph, amphibole; Chl, chlorite; Ol, olivine; Opx, orthopyroxene; Serp, serpentine.

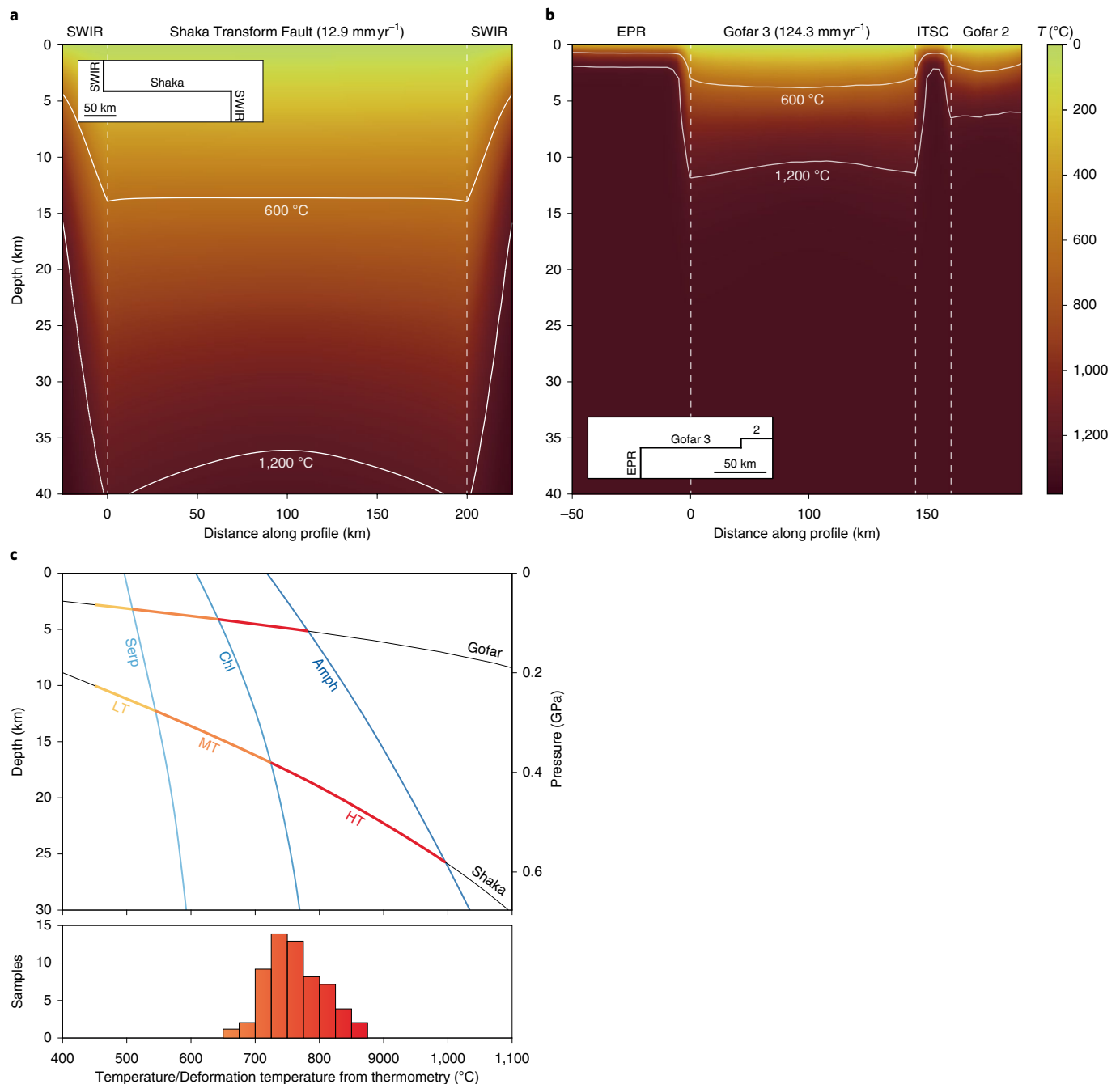


Fig. 2 | Thermal models and hydrous mineralogy of OTFs. **a, b**, Shaka transform fault (slip rate 12.9 mm yr⁻¹) (**a**) and Gofar segments 2 and 3 (slip rate 124.3 mm yr⁻¹) (**b**). Profiles run parallel to the ridge-fault-ridge system (insets) (see Extended Data Table 1 for model parameters). **c**, Top: fault centre geotherms and hydrous mineral stability limits for amphibole, chlorite and serpentine, which distinguish the LT, MT and HT mylonites. Bottom: thermometry calculations based on the calcium in orthopyroxene (Opx) in the SWIR mylonites¹³ constrain the LT limit of ductile recrystallization.

Fault rheology and fluid-deformation feedbacks

The mechanisms that govern ductile deformation in OTF mylonites and their protolith can be interpreted from the mylonite microstructures¹². Prior to deformation in the fault zone, the mantle protolith was assumed to be coarse-grained peridotite formed by melt extraction within the asthenosphere (for example, Fig. 3a insets). This starting point corresponds to the pressure (depth) at which the fault is at the mantle potential temperature in the thermal models (Methods). We use the grain size and pressure–temperature conditions to construct deformation mechanism maps for the protolith on Shaka and Gofar using olivine flow laws^{18–20} (Extended Data Figs. 1

and 2). The flow-law equations and parameters are provided in Extended Data Table 2. For both faults, the protolith is expected to deform by a combination of dislocation creep and grain boundary sliding at strain rates of $\sim 10^{-9}$ – 10^{-11} s⁻¹.

Once fluids are introduced into the fault zone, weak, fine-grained shear zones can form via a positive feedback loop. The presence of fluids weakens olivine, which increases the strain rate and decreases the grain size^{21–24}. Fluids are drawn into rapidly deforming zones²⁵, where the formation of hydrous phases further weakens olivine through grain-size reduction due to phase boundary pinning^{12,26}. The formation of mylonites from the mantle protolith represents

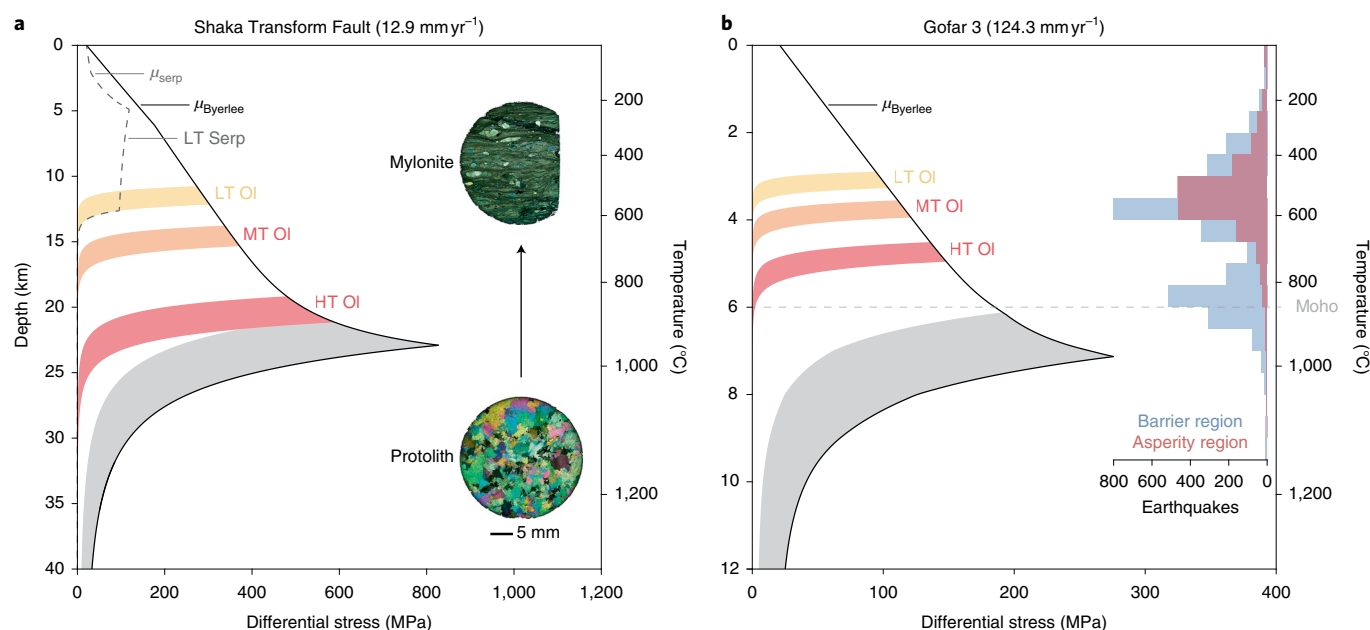


Fig. 3 | Strength-depth profiles for slow- and fast-slipping OTFs. The intersection of each flow law with the friction lines represents the transition from brittle to ductile behaviour. The lines μ_{Byerlee} and μ_{serp} represent the frictional strengths of olivine and serpentine (Methods). Each coloured region corresponds to flow laws calculated over the range of the estimate deformation conditions (Supplementary Table 4). **a**, Shaka transform fault (slip rate 12.9 mm yr^{-1}). Insets: characteristic protolith and mylonite microstructures. **b**, Gofar segment 3 (slip rate 124.3 mm yr^{-1}). Histograms show the earthquake count in the asperity (red) and barrier (blue) regions from the 2008 OBS experiment^{5,9}. The Moho depth was determined by seismic tomography⁶.

a reduction in grain size of 2–3 orders of magnitude. This process results in a change in the olivine deformation mechanism from grain-size-insensitive to grain-size-sensitive creep¹², and thereby strengthens the fluid-deformation feedbacks.

Using the pressure–temperature conditions estimated for the mylonites, we constructed deformation mechanism maps for the LT, MT and HT regions using the flow laws for olivine and serpentine (Extended Data Figs. 1 and 2). Amphibole and chlorite flow laws have not been developed. Although laboratory tests²⁷ and the analyses of exhumed mantle shear zones²⁸ suggest that amphibole is stronger than olivine, in OTF mylonites, the proportion of amphibole inversely correlates with olivine grain size^{12,13}. This indicates that the presence of amphibole weakens peridotite by pinning the olivine grain boundaries. At the average grain size of the fine-grained zones within the mylonites (1–10 μm), olivine deformation occurs entirely within the diffusion-creep field and serpentine deforms by dislocation creep²⁹. Assuming iso-stress deformation³⁰, the estimated strain rates for the mylonites span over ten orders of magnitude ($\sim 10^{-5}$ – 10^{-17} s^{-1} ; Extended Data Fig. 3).

Brittle–ductile deformation and seawater infiltration

To estimate the depth extent of brittle deformation and seawater infiltration, we calculated strength–depth profiles for Shaka and Gofar using the modelled geotherms, measured grain sizes and estimated strain rates (Fig. 3). For each flow law, we considered the transition from brittle (pressure dependent) to ductile (temperature dependent) behaviour as the depth at which the flow law intersects the modified friction-effective stress line (Methods and Extended Data Fig. 4). The protolith had an olivine grain size of ~ 1 – 5 mm and deformed by a combination of dislocation creep and grain-boundary sliding (Extended Data Figs. 1 and 2). Under these conditions, olivine transitions from brittle to ductile behaviour at 22–24 km on Shaka and 6–7 km on Gofar. This represents the base of the brittle–ductile zone and corresponds to a temperature range of ~ 900 – $1,000^\circ\text{C}$.

Although our rheological model indicates that the brittle deformation of olivine is possible at $1,000^\circ\text{C}$ at slow (interseismic) strain rates, the amphibole minerals that form during hydration of the HT mylonites are only stable at lower temperatures (Fig. 2c). Therefore, the stability limit of amphibole represents a minimum estimate for the depth limit of seawater–mantle interactions on OTFs. Hydrothermal fluids may percolate deeper, down to the base of the brittle–ductile transition, but leave no mineralogical signature as no hydrous phases associated with peridotite are stable at $>900^\circ\text{C}$. The Shaka mylonites contain healed fractures filled with fluid inclusions within porphyroclasts, which suggests that hydration occurred at temperatures beyond amphibole stability in the coarse-grained protolith¹².

The formation of hydrous peridotite mylonites results in a wide temperature range over which brittle and ductile deformation are coeval. The base of this zone is defined by olivine in the HT mylonites, which undergoes a transition from brittle to ductile behaviour at ~ 700 – 900°C . The shallow extent of the brittle–ductile zone is defined by the rheology of serpentine, the weakest phase in the LT mylonites²⁹. Serpentine is frictionally weak compared with olivine (Byerlee’s law)^{31–33}. As its frictional strength depends on a variety of factors, we used a depth-dependent friction coefficient that ranged from 0.1 to 0.6 based on values determined in experimental studies^{31–33} (Supplementary Information). The intersection of the serpentine flow law with the serpentine friction line yielded a temperature range of ~ 200 – 400°C . The corresponding depth range of the brittle–ductile transition zone in which LT-to-HT mylonites can form is 4–22 km on Shaka and 1–5 km on Gofar.

Controls on the extent of seismicity on OTFs

The best geophysical constraints on the depth extent of brittle deformation on OTFs are earthquakes recorded during OBS deployments on Gofar, Discovery and Quebrada on the fast-spreading East Pacific Rise (EPR)^{5,6,9} and Blanco on the intermediate-spreading Juan de Fuca Ridge (JDF)⁸ (Fig. 1a). These studies show along-strike

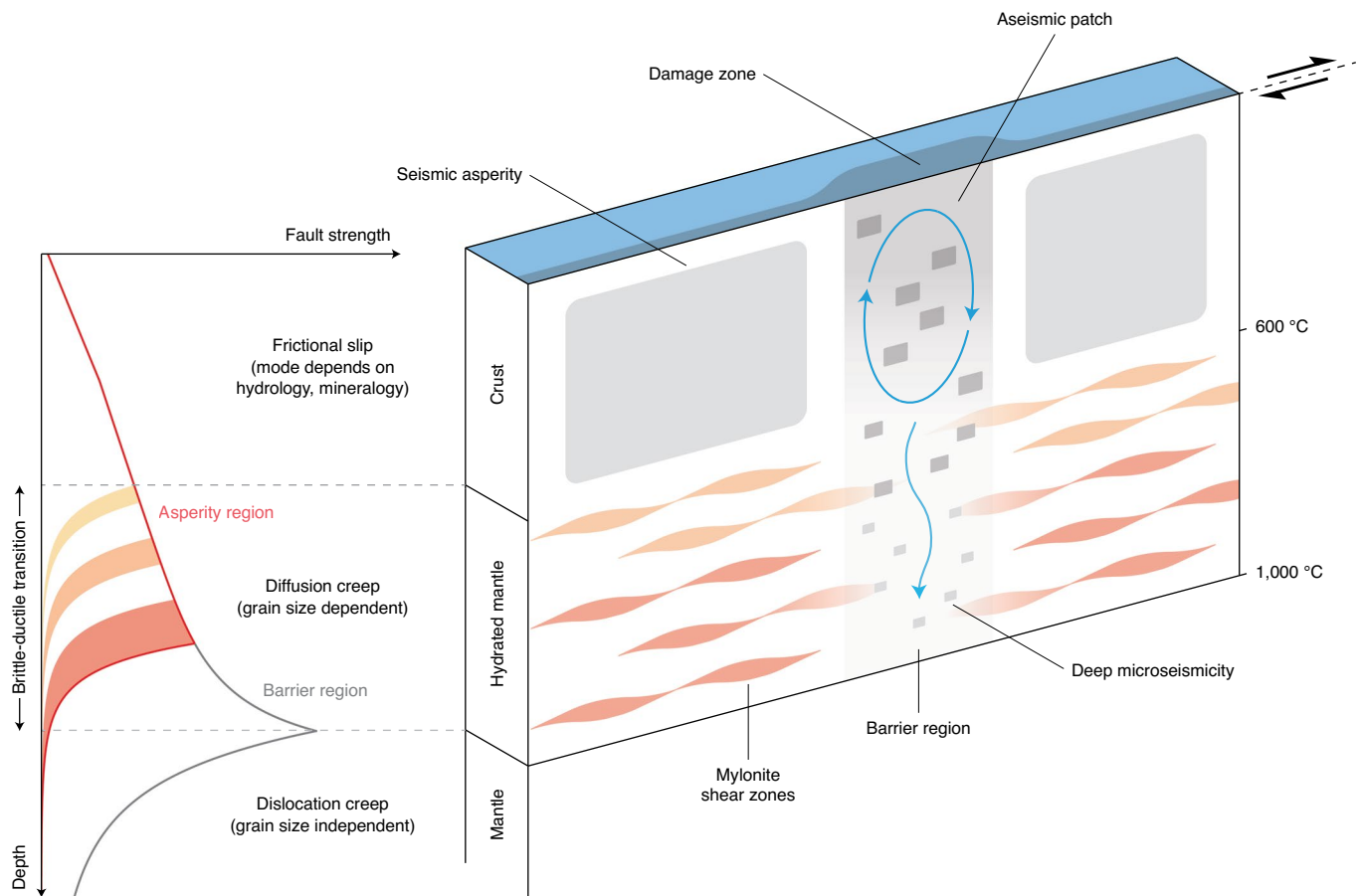


Fig. 4 | Vertical and along-strike variations in seismicity on OTFs. Fully coupled seismic patches (large grey areas) are limited in vertical extent by the 600 °C isotherm, below which weak mylonite shear zones (coloured bands) can form. Asperity regions are separated by barrier regions that slip through aseismic creep and microearthquakes on small, distributed seismic patches (small grey areas) that extend into the mantle lithosphere. Over time, these rupture barriers may become asperity patches as mantle rheology and mineralogy evolve with progressive hydration and strain.

variations in the maximum depth of seismicity. On some fault patches, earthquakes are limited to depths that correspond to <600–700 °C in modelled thermal structure, whereas on others the seismicity extends into the mantle up to 1,000 °C (ref. 6). The thermal limit of seismicity determined in OBS studies is consistent with our estimates of the temperature of the brittle–ductile transition from the rheology of coarse-grained peridotite and mantle mylonites from Shaka. LT and HT mylonites from the Garrett transform fault (Fig. 1b) show nearly identical microstructures to those of the Shaka mylonites (Fig. 1c,d), which indicates that the same fluid-deformation feedbacks that occur on slow-slipping transforms also take place on fast-slipping transforms^{34,35}.

Our calculations demonstrate that along-strike differences in mantle hydration may result in spatiotemporal variations in the mode of slip on OTFs. Progressive hydration and the formation of weak mantle mylonites increases the contribution of aseismic creep, which decreases seismic coupling in the mantle. OBS observations of along-strike variations in the mode of slip on fast- and intermediate-slipping transform faults^{5,7,36,37} support this model. On asperity patches, where large, quasi-periodic ruptures occur, seismicity is limited to the crust, whereas in the barrier regions, where large ruptures stop, microseismicity extends into the mantle^{5,6}. Seismological studies of the Gofar OBS dataset show low compressional wave velocities and low stress drops in the barrier regions, which are attributed to enhanced hydrothermal circulation and alteration caused by fault zone damage^{9,38}. Models of earthquake

cycles on Gofar show that enhanced dilatancy in damage zones results in aseismic transients and rupture arrest in the seismogenic zone¹¹. This explains along-strike variations in the mode of slip in the shallow part of the fault, but does not explain differences in the depth extent of seismicity between the asperity and barrier zones, as dilatancy is inhibited at higher pressures.

Based on our rheological model, we propose that barrier regions on OTFs correspond to sections of the fault in which hydrated mylonite shear zones are not pervasive at depth (Fig. 4). These regions, instead, contain relatively coarse-grained peridotite, which is expected to sustain brittle behaviour at greater pressure–temperature conditions. This idea is supported by our observations that coarse-grained peridotites recovered from SWIR transform faults exhibit a greater fracture density and hydrothermal alteration compared with that of mylonites^{12,13}, consistent with geophysical interpretations of the Gofar barrier region¹⁰. The Gofar OBS data also show that seismicity on asperity regions is limited to temperatures <600–700 °C (ref. 5), in agreement with our estimate of the thermal limit of brittle deformation in regions in which MT–HT mylonites would form (Fig. 3b). This implies that asperity patches are underlain by weak, hydrated shear zones in which slip is accommodated by relatively rapid, aseismic creep. Accumulated aseismic slip in these shear zones may be responsible for loading the shallow portion of the asperity regions, as well as the deep portion of adjacent coarser-grained regions, which possibly drives large ruptures in the asperity regions and deep microseismicity in the barrier regions.

Our results demonstrate that vertical and along-strike variations in the extent of seismicity on OTFs can be explained by the impacts of deep seawater circulation on the fault rheology. The formation of hydrous mantle mylonites over a broad temperature range (300–900°C) allows fault slip to be accommodated by aseismic creep. Although variations in dilatancy can explain the slip dynamics of seismic and aseismic patches in the crust¹¹, the formation of these patches and their extent within the mantle are determined by seawater–rock interactions that extend to the brittle–ductile transition. Therefore, a new generation of OTF models is needed that incorporate constraints on seawater infiltration from fault rocks, as well as feedbacks between hydration, thermal structure and fault rheology. Allowing the multimodal slip behaviour observed on OTFs^{36–38} to evolve dynamically over time will further our understanding of how fluid flow in fault zones contributes to spatiotemporal variations of slip on plate interfaces.

Online content

Any methods, additional references, Nature Research reporting summaries, source data, extended data, supplementary information, acknowledgements, peer review information; details of author contributions and competing interests; and statements of data and code availability are available at <https://doi.org/10.1038/s41561-021-00778-1>.

Received: 2 December 2019; Accepted: 25 May 2021;

Published online: 5 August 2021

References

- Wiens, D. A. & Stein, S. Age dependence of oceanic intraplate seismicity and implications for lithospheric evolution. *J. Geophys. Res.* **88**, 6455–6468 (1983).
- Chen, W.-P. & Molnar, P. Focal depths of intracontinental and intraplate earthquakes and their implications for the thermal and mechanical properties of the lithosphere. *J. Geophys. Res.* **88**, 4183–4214 (1983).
- Abercrombie, R. E. & Ekström, G. Earthquake slip on oceanic transform faults. *Nature* **410**, 74–77 (2001).
- Boettcher, M. S., Hirth, G. & Evans, B. Olivine friction at the base of oceanic seismogenic zones. *J. Geophys. Res.* **112**, B01205 (2007).
- McGuire, J. J. et al. Variations in earthquake rupture properties along the Gofar transform fault, East Pacific Rise. *Nat. Geosci.* **5**, 336–341 (2012).
- Roland, E., Lizarralde, D., McGuire, J. J. & Collins, J. A. Seismic velocity constraints on the material properties that control earthquake behavior at the Quebrada–Discovery–Gofar transform faults, East Pacific Rise. *J. Geophys. Res.* **117**, B11102 (2012).
- Wolfson-Schwehr, M., Boettcher, M. S., McGuire, J. J. & Collins, J. A. The relationship between seismicity and fault structure on the Discovery transform fault, East Pacific Rise. *Geochem. Geophys. Geosyst.* **15**, 3698–3712 (2014).
- Kuna, V. M., Nábělek, J. L. & Braunmiller, J. Mode of slip and crust–mantle interaction at oceanic transform faults. *Nat. Geosci.* **12**, 138–142 (2019).
- Froment, B. et al. Imaging along-strike variations in mechanical properties of the Gofar transform fault, East Pacific Rise. *J. Geophys. Res.* **119**, 7175–7194 (2014).
- Guo, H., Zhang, H. & Froment, B. Structural control on earthquake behaviors revealed by high-resolution V_p/V_s imaging along the Gofar transform fault, East Pacific Rise. *Earth Planet. Sci. Lett.* **499**, 243–255 (2018).
- Liu, Y., McGuire, J. J. & Behn, M. D. Aseismic transient slip on the Gofar transform fault, East Pacific Rise. *Proc. Natl Acad. Sci. USA* **117**, 10188–10194 (2020).
- Kohli, A. H. & Warren, J. M. Evidence for a deep hydrologic cycle on oceanic transform faults. *J. Geophys. Res.* **125**, B017751 (2020).
- Prigent, C., Warren, J. M., Kohli, A. H. & Teyssier, C. Fracture-mediated deep seawater flow and mantle hydration on oceanic transform faults. *Earth Planet. Sci. Lett.* **532**, 115988 (2020).
- Connolly, J. A. D. The geodynamic equation of state: what and how. *Geochem. Geophys. Geosyst.* **10**, Q10014 (2009).
- Guillot, S., Schwartz, S., Reynard, B., Agard, P. & Prigent, C. Tectonic significance of serpentinites. *Tectonophysics* **646**, 1–19 (2015).
- Fumagalli, P., Zanchetta, S. & Poli, S. Alkali in phlogopite and amphibole and their effects on phase relations in metasomatized peridotites: a high-pressure study. *Contrib. Mineral. Petrol.* **158**, 723–737 (2009).
- Chernosky, J. V. Jr, Berman, R. G. J. & Jenkins, D. M. The stability of tremolite: new experimental data and a thermodynamic assessment. *Am. Mineral.* **83**, 726–738 (1998).
- Hirth, G. & Kohlstedt, D. In *Inside the Subduction Factory* (ed. Eiler, J.) 83–105 (AGU, 2003).
- Hansen, L. N., Zimmerman, M. E. & Kohlstedt, D. L. Grain boundary sliding in San Carlos olivine: flow law parameters and crystallographic-preferred orientation. *J. Geophys. Res.* **116**, B08201 (2011).
- Ohuchi, T. et al. Dislocation-accommodated grain boundary sliding as the major deformation mechanism of olivine in the Earth's upper mantle. *Sci. Adv.* **1**, e1500360 (2015).
- Carter, N. L. & Avé Lallemant, H. G. High temperature flow of dunite and peridotite. *Geol. Soc. Am. Bull.* **81**, 2181–2202 (1970).
- Karato, S.-I., Paterson, M. & Fitzgerald, D. Rheology of synthetic olivine aggregates: Influence of grain size and water. *J. Geophys. Res.* **91**, 8151–8176 (1986).
- Chopra, P. N. & Paterson, M. S. The experimental deformation of dunite. *Tectonophysics* **78**, 453–473 (1981).
- Hirth, G. & Kohlstedt, D. L. Water in the oceanic upper mantle: implications for rheology, melt extraction and the evolution of the lithosphere. *Earth Planet. Sci. Lett.* **144**, 93–108 (1996).
- Fussey, F., Regenauer-Lieb, K., Liu, J., Hough, R. M. & De Carlo, F. Creep cavitation can establish a dynamic granular fluid pump in ductile shear zones. *Nature* **459**, 974–977 (2009).
- Précigout, J., Prigent, C., Palasse, L. & Pochon, A. Water pumping in mantle shear zones. *Nat. Commun.* **8**, 15736 (2017).
- Getsinger, A. J. & Hirth, G. Amphibole fabric formation during diffusion creep and the rheology of shear zones. *Geology* **42**, 535–538 (2014).
- Tommasi, A., Langone, A., Padrón-Navarra, J. A., Zanetti, A. & Vauchez, A. Hydrous melts weaken the mantle, crystallization of pargasite and phlogopite does not: insights from a petrostructural study of the Finero peridotites, southern Alps. *Earth Planet. Sci. Lett.* **477**, 59–72 (2017).
- Hilaret, N. et al. High-pressure creep of serpentine, interseismic deformation, and initiation of subduction. *Science* **318**, 1910–1913 (2007).
- Platt, J. P. & Behr, W. M. Grain size evolution in ductile shear zones: implications for strain localization and the strength of the lithosphere. *J. Struct. Geol.* **33**, 537–550 (2011).
- Reinen, L. A., Weeks, J. D. & Tullis, T. E. The frictional behavior of lizardite and antigorite serpentinites: experiments, constitutive models, and implications for natural faults. *Pure Appl. Geophys.* **143**, 317–358 (1994).
- Moore, D. E., Lockner, D. A., Ma, S., Summers, R. & Byerlee, J. D. Strengths of serpentinite gouges at elevated temperatures. *J. Geophys. Res.* **102**, 14787–14801 (1997).
- Moore, D. E. & Lockner, D. A. Frictional strengths of talc–serpentine and talc–quartz mixtures. *J. Geophys. Res.* **116**, B01403 (2011).
- Cannat, M., Bideau, D. & Hébert, R. Plastic deformation and magmatic impregnation in serpentinitized ultramafic rocks from the Garrett transform fault (East Pacific Rise). *Earth Planet. Sci. Lett.* **101**, 216–232 (1990).
- Constantin, M. Gabbroic intrusions and magmatic metasomatism in harzburgites from the Garrett transform fault: Implications for the nature of the mantle–crust transition at fast-spreading ridges. *Contrib. Mineral. Petrol.* **136**, 111–130 (1999).
- Aderhold, K. & Abercrombie, R. E. The 2015 M_w 7.1 earthquake on the Charlie–Gibbs transform fault: repeating earthquakes and multimodal slip on a slow oceanic transform. *Geophys. Res. Lett.* **43**, 6119–6128 (2016).
- Wolfson-Schwehr, M. & Boettcher, M. S. In *Transform Plate Boundaries and Fracture Zones* (ed. Duarte, J. C.) 21–59 (Elsevier, 2019).
- Moyer, P. A., Boettcher, M. S., McGuire, J. J. & Collins, J. A. Spatial and temporal variations in earthquake stress drop on Gofar Transform Fault, East Pacific Rise: implications for fault strength. *J. Geophys. Res.* **123**, 7722–7740 (2018).

Publisher's note Springer Nature remains neutral with regard to jurisdictional claims in published maps and institutional affiliations.

© The Author(s), under exclusive licence to Springer Nature Limited 2021

Methods

Thermal model. Thermal models were constructed using the finite element software package COMSOL Multiphysics (v.4.2a). In the models, ductile deformation follows a viscoplastic, temperature-dependent flow law, which has the form:

$$\dot{\epsilon} = A\sigma^n e^{-E/RT} \quad (1)$$

where the strain rate $\dot{\epsilon}$ is a function of the pre-exponential constant A , differential stress σ , stress exponent n , activation energy E , molar gas constant R and temperature T .

Brittle deformation follows Byerlee's law³⁹, in which the maximum shear stress τ_{\max} is a function of the friction coefficient μ , normal stress σ_n and cohesive strength τ_0 :

$$\tau_{\max} = \mu\sigma_n + \tau_0 \quad (2)$$

The inclusion of a temperature-dependent viscosity and a frictional failure law causes an enhanced upwelling below the transform fault compared with that in thermal models that do not incorporate deformation^{34,40}. This results in a warmer thermal structure overall, although the isotherms do not converge upwards when approaching the ridge axis, which creates a lower thermal gradient near the ridge⁴¹. The estimated mantle potential temperature for Shaka is 1,380 °C (ref. ⁴²), which is relatively high due to the passage of the Bouvet mantle plume⁴³. For Gofar, the mantle potential temperature is assumed to be slightly lower, at 1,300 °C (ref. ⁴¹). The thermal model parameters are provided in Extended Data Table 1. The ridge and fault geometry in the models is based on bathymetry data. Shaka is modelled as a single, 200-km-long segment, and Gofar is discretized into three fault segments separated by small spreading ridges⁶.

The ductile rheology is a dislocation creep flow law for dry olivine¹⁸, which is grain-size insensitive. The fine-grained layers of the Shaka mylonites are predicted to deform by wet diffusion creep (which is grain-size sensitive), but the model is not currently designed to allow for the ductile flow law to vary spatially or temporally. The thermal model also does not account for deep hydrothermal circulation. The amount of cooling due to shallow hydrothermal circulation results in a ~1–2 km deepening in the thermal structure⁴⁴, so incorporating deeper fluid infiltration would further deepen (cool) the thermal structure. Grain-size-sensitive creep and enhanced hydrothermal circulation should be incorporated in future models to more accurately reflect the conditions of mylonite deformation. In addition, although secondary phases (pyroxene and amphibole) are important to mylonite deformation¹², our calculations only consider a pure olivine system. At present, flow laws for olivine–pyroxene or olivine–amphibole systems at mantle compositions are not known, although experiments have been conducted on more Fe-rich olivine–pyroxene mixtures⁴⁵. As the extrapolation of this flow law to mantle compositions is unknown, the pure olivine flow law remains the best option to assess the impacts of strain localization and hydration on fault rheology. However, our observation that the presence of hydrous phases weakens peridotite^{12,13} suggests that the brittle–ductile transition may be shallower than predicted by olivine flow laws.

Strength–depth profiles. Brittle deformation is represented by frictional equilibrium for transform faults⁴⁶, in which the strength of the lithosphere is the differential stress:

$$(\sigma_1 - \sigma_3) = \mu'(\sigma_n - P_f) + \tau_0 \quad (3)$$

where P_f is the pore fluid pressure. The parameter μ' represents the minimum stress conditions to initiate fault slip, given a coefficient of friction μ :

$$\mu' = 2\mu/(\mu^2 + 1)^{1/2} \quad (4)$$

The effective overburden pressure, σ_v , with depth z is given by:

$$\sigma_v = \rho gz(1 - \lambda) \quad (5)$$

in which ρ is the density, g the acceleration due to gravity and λ the ratio of P_f to the overburden. Following previous studies⁴⁷, we assumed that the fault normal stress is equal to the overburden. This is a reasonable assumption given that OTFs are in a normal/strike–slip stress state, so the vertical stress (overburden) and maximum horizontal stress are similar in magnitude. We employed a modified effective pressure law to account for the temperature dependence of viscous creep (Supplementary Equation (4)), which is discussed in detail in the Supplementary Information. In accordance with Byerlee's law³⁹, $\mu = 0.85$ in the shallow crust ($P < 0.2$ GPa) and $\mu = 0.6$ at depth. For Fig. 3, we considered conditions of hydrostatic pore pressure ($\lambda = 0.4$) and the friction coefficients for olivine, $\mu = 0.6$ (ref. ⁴), and serpentine, $\mu = 0.1$ – 0.6 . The frictional strength of serpentine is dependent on the mineral polymorph, slip velocity and pressure–temperature, so we used a depth-dependent frictional strength based on relevant experimental data^{31–33} (Supplementary Information).

Ductile deformation is represented by a viscoplastic, temperature-dependent flow law similar to equation (1). Depending on the state of the fault zone (protolith

or mylonite), the strain rate also depends on water content and grain size. The general form of the flow law for dislocation creep and diffusion creep is:

$$\dot{\epsilon} = A\sigma^n d^p C_{\text{OH}}^r e^{-(E+PV)/RT} \quad (6)$$

in which d is the grain size, p is the grain-size exponent, C_{OH} is the water concentration, r is the water concentration exponent, P is pressure and V is the activation volume. The form of the flow law for LT plasticity is:

$$\dot{\epsilon} = A\sigma^n d^p C_{\text{OH}}^r e^{\left[-\frac{E}{RT}\left(1 - \frac{\sigma}{\sigma_p}\right)^q\right]} \quad (7)$$

where σ_p is the Peierls stress and p and q are non-dimensional parameters that describe dislocation motion. The flow law parameters are provided in Extended Data Table 2.

Data availability

OTF mylonite and OBS deployment locations are provided in Supplementary Information Table 1. OTF mylonite compositional data is available at EarthChemLibrary⁴⁸. The Gofar seismic data is available from the IRIS Data Management Center (https://www.fdsn.org/networks/detail/ZD_2007/). Source data are provided with this paper.

Code availability

The codes used to generate the thermal models, deformation mechanism maps and strength–depth profiles can be accessed at <https://github.com/ahkohli/OTFs>.

References

- Byerlee, J. Friction of rocks. *Pure Appl. Geophys.* **116**, 615–626 (1978).
- Stein, C. A. & Stein, S. A model for the global variation in oceanic depth and heat flow with lithospheric age. *Nature* **359**, 123–128 (1992).
- Behn, M. D., Boettcher, M. S. & Hirth, G. Thermal structure of oceanic transform faults. *Geology* **35**, 307–310 (2007).
- Dalton, C. A., Langmuir, C. H. & Gale, A. Geophysical and geochemical evidence for deep temperature variations beneath mid-ocean ridges. *Science* **344**, 80–83 (2014).
- Hartnady, C. J. H. & le Roex, A. P. Southern Ocean hotspot tracks and the Cenozoic absolute motion of the African, Antarctic, and South American plates. *Earth Planet. Sci. Lett.* **75**, 245–257 (1985).
- Roland, E., Behn, M. D. & Hirth, G. Thermal-mechanical behavior of oceanic transform faults: implications for the spatial distribution of seismicity. *Geochim. Geophys. Res.* **11**, Q07001 (2010).
- Tasaka, M., Hiraga, T. & Zimmerman, M. E. Influence of mineral fraction on the rheological properties of forsterite + enstatite during grain-size-sensitive creep: 2. Deformation experiments. *J. Geophys. Res.* **118**, 3991–4012 (2013).
- Sibson, R. H. Frictional constraints on thrust, wrench and normal faults. *Nature* **249**, 542–544 (1974).
- Beeler, N. M., Hirth, G., Thomas, A. & Bürgmann, R. Effective stress, friction, and deep crustal faulting. *J. Geophys. Res.* **121**, 1040–1059 (2015).
- Kohli, A. H. & Warren, J. M. *X-ray diffraction data on peridotite mylonites from the Shaka Transform Fault, Southwest Indian Ridge, Version 1.0* (Interdisciplinary Earth Data Alliance, accessed 13 August 2019); <https://doi.org/10.1594/IEDA/111356>

Acknowledgements

We thank C. Teyssier, S. Birner, K. Kumamoto, L. Hansen, M. Boettcher, M. Behn, J. McGuire and G. Hirth for helpful discussions. This work was supported by a NSF Graduate Research Fellowship to A.K. and NSF grants EAR-1347696, EAR-1619880 and OCE-1832868 to J.M.W.

Author contributions

A.K., C.P. and J.M.W. performed analyses of the mylonite samples. M.W.-S. built the thermal models. C.P. conducted the geochemical measurements. A.K. performed the rheology calculations. All the authors discussed the results and contributed to writing the manuscript.

Competing interests

The authors declare no competing interests.

Additional information

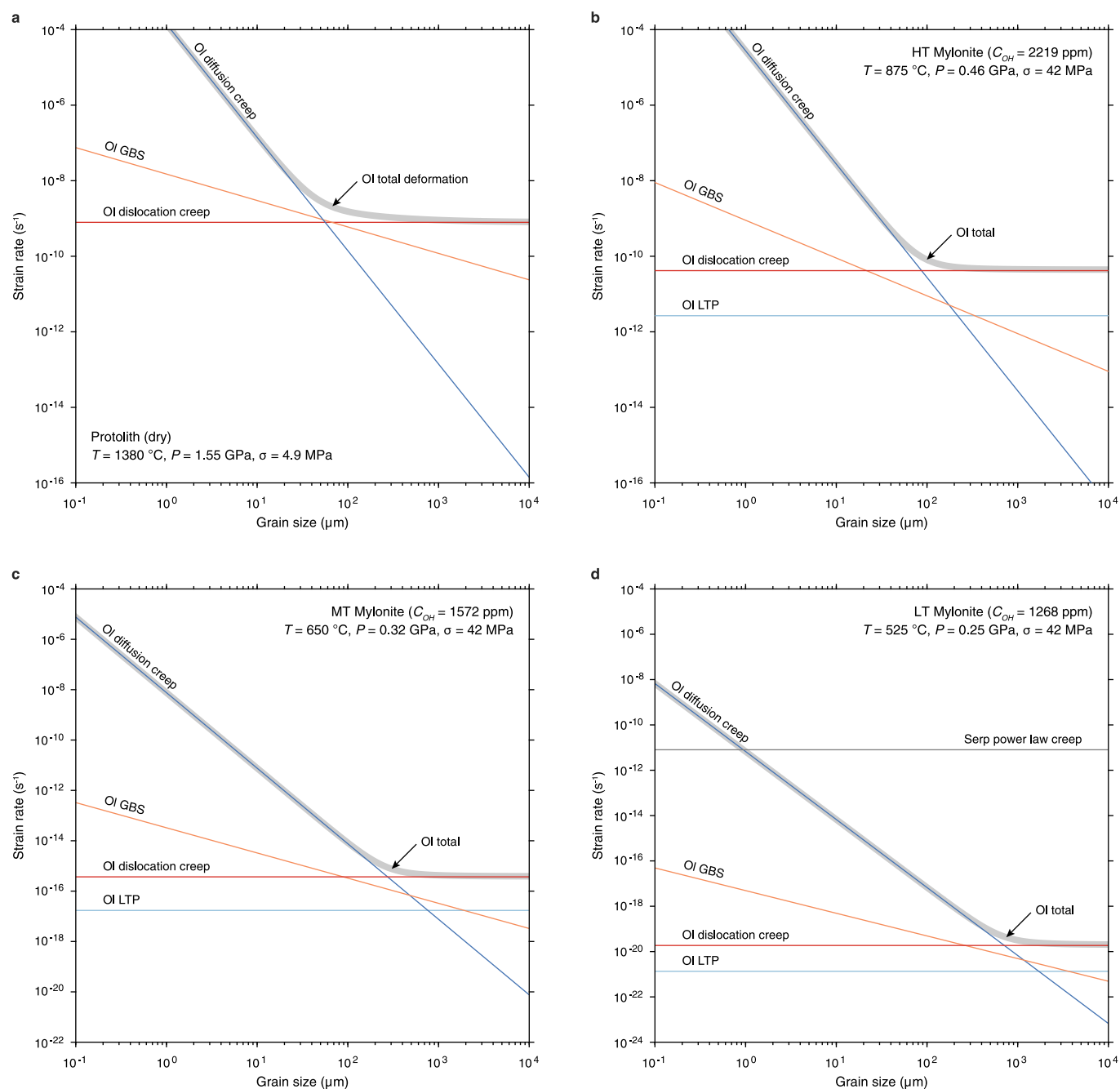
Extended data is available for this paper at <https://doi.org/10.1038/s41561-021-00778-1>.

Supplementary information The online version contains supplementary material available at <https://doi.org/10.1038/s41561-021-00778-1>.

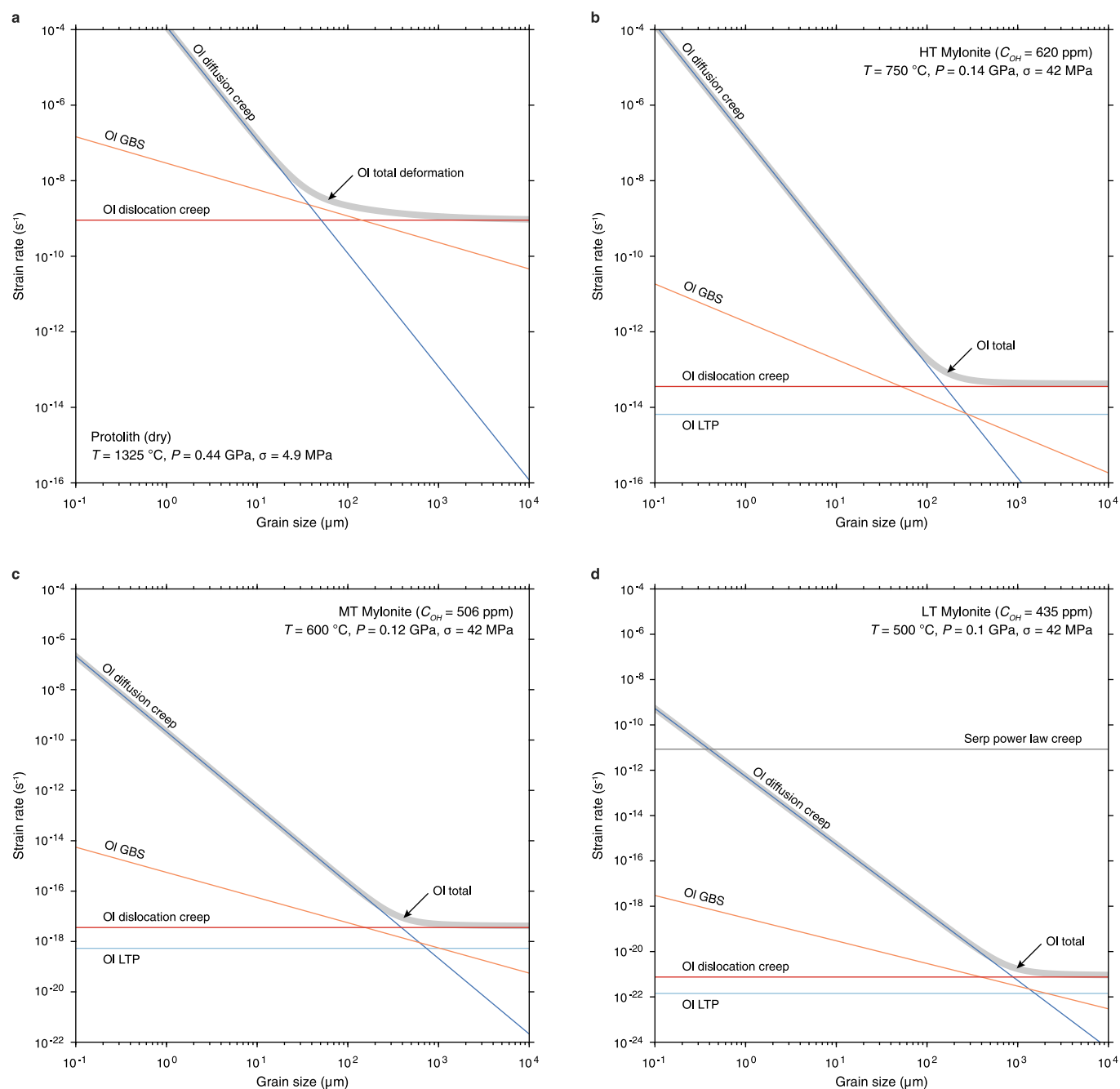
Correspondence and requests for materials should be addressed to A.K. or J.M.W.

Peer review information *Nature Geosciences* thanks the anonymous reviewer(s) for their contribution to the peer review of this work. Primary Handling Editor: Stefan Lachowycz.

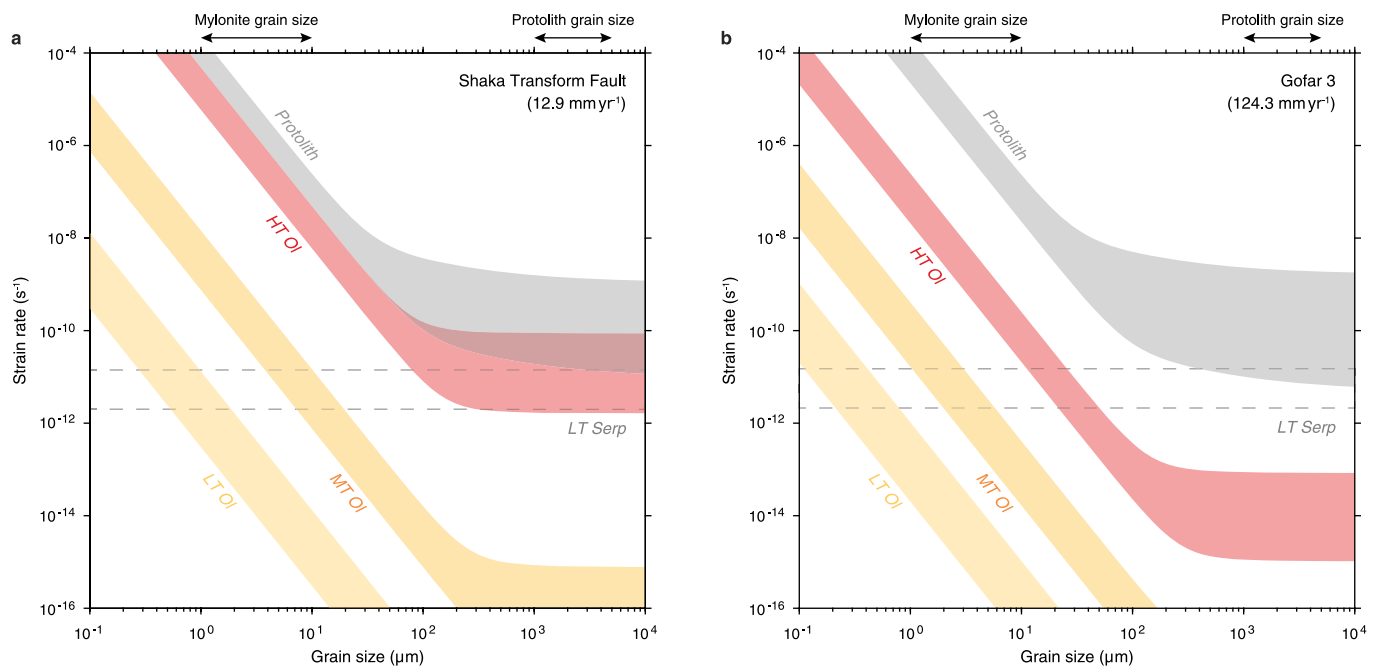
Reprints and permissions information is available at www.nature.com/reprints.



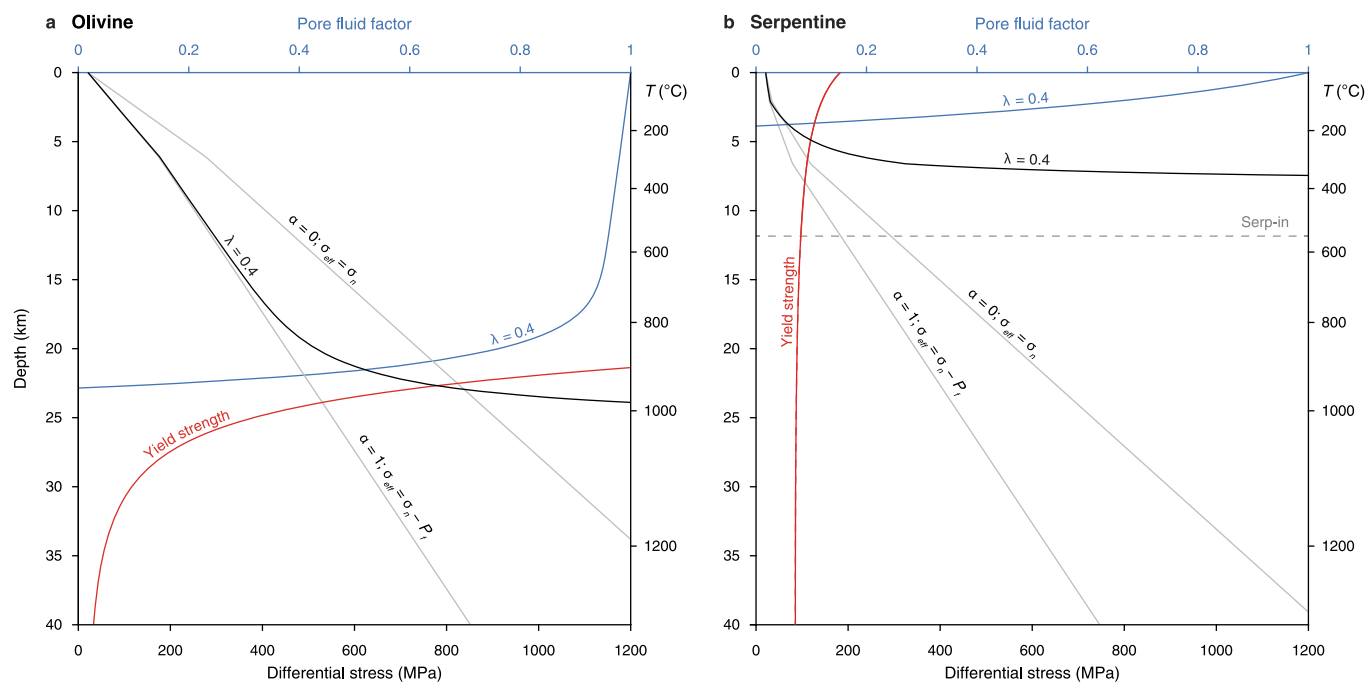
Extended Data Fig. 1 | Deformation mechanism maps for Shaka transform fault. Maps were generated using the flow law parameters in Extended Data Table 2. **a**, Protolith. **b**, HT mylonite. **c**, MT mylonite. **d**, LT mylonite.



Extended Data Fig. 2 | Deformation mechanism maps for Gofar transform fault. Maps were generated using the flow law parameters in Extended Data Table 2. **a**, Protolith. **b**, HT mylonite. **c**, MT mylonite. **d**, LT mylonite.



Extended Data Fig. 3 | Composite deformation mechanism maps for (a) Shaka and (b) Gofar transform faults. The total strain rate is the arithmetic sum of the strain rates from each deformation mechanism (that is, Ol total in Extended Data Figs. 1, 2). The ranges for each curve represent uncertainty in the pressure-temperature estimates for deformation.



Extended Data Fig. 4 | Modified friction-effective stress relationship for olivine and serpentine. Modified friction-effective stress relationship for (a) olivine and (b) serpentine calculated using the Shaka geotherm (Fig. 2a) and hydrostatic pore fluid pressure ($\lambda=0.4$). The pore fluid factor, α , decreases from 1 at the surface to 0 at the brittle-ductile transition as the normal stress on asperity contacts nears the yield strength.

Extended Data Table 1 | Material properties and boundary conditions for fault thermal models (Fig. 2a,b)

Material properties		
Parameter	Value	
Mantle lithosphere density	3300 kg·m ⁻³	
Water density	1000 kg·m ⁻³	
Reference viscosity	10 ¹⁹ Pa·s	
Maximum viscosity	10 ²⁴ Pa·s	
Thermal conductivity	3 W·m ⁻¹ ·K ⁻¹	
Specific heat	1000 J·kg ⁻¹ ·K ⁻¹	
Gas constant	8.3145 J·mol ⁻¹ ·K ⁻¹	
Olivine flow law ¹⁸	Dry dislocation creep	
Coefficient of friction ³⁹	0.85	
Cohesive strength ⁴	20 MPa	
Gravitational acceleration	9.81 m·s ⁻²	

Boundary conditions		
Parameter	Shaka	Gofar 3
Length of fault segment	200 km	95 km
Length of ridge segments	50 km	50 km, 14 km
Full spreading rate	12.92 mm·yr ⁻¹	124.55 mm·yr ⁻¹
Surface temperature	0 °C	0 °C
Mantle potential temperature ⁴²	1380 °C	1300 °C

Extended Data Table 2 | Flow laws and constitutive parameters used in deformation mechanism maps (Extended Data Figs. 1, 2) and strength-depth profiles (Fig. 3). *The value of A has been adjusted from the original references to account for revised estimates of the water content in the experimental samples. GBS - Grain boundary sliding; LTP - Low temperature plasticity

Olivine flow laws

Mechanism	n	p	q	r	* A ($\mu\text{m}^{-p}\cdot\text{s}^{-1}\cdot\text{MPa}^{-n}$)	E ($\text{kJ}\cdot\text{mol}^{-1}$)	V ($10^{-6}\cdot\text{m}^3\cdot\text{mol}^{-1}$)	σ_P (GPa)	Reference
Dry Diffusion creep	1	-3	—	—	1.5e9	375	2	—	18
	—	—	—	—	3.98e7	—	—	—	19
Dry GBS	2.9	-0.7	—	—	5.01e4	445	18	—	19
Dry dislocation creep	3.5	0	—	—	1.10e4	520	14	—	18
Dry LTP	2	0.5	1	—	1.40e-7	320	0	5.9	50
Wet diffusion creep	1	-3	—	1	4.00e5	335	4	—	18
Wet GBS	3	-1	—	1.25	1.29e1	423	18	—	20
Wet dislocation creep	3.5	0	—	1.2	3.00e1	480	11	—	18
Wet LTP	2	0.75	1	—	1.26e7	518	—	2.1	49

Serpentine flow laws

Mechanism	n	p	q	r	* A ($\mu\text{m}^{-p}\cdot\text{s}^{-1}\cdot\text{MPa}^{-n}$)	E ($\text{kJ}\cdot\text{mol}^{-1}$)	V ($10^{-6}\cdot\text{m}^3\cdot\text{mol}^{-1}$)	σ_P (GPa)	Reference
Wet power law creep	3.8	0	—	—	1.8e-17	9	3	—	29